



The phase space of last glacial inception for the Northern Hemisphere from coupled ice and climate modelling

Taimaz Bahadory¹, Lev Tarasov¹, and Heather Andres¹

¹Memorial University of Newfoundland and Labrador

Correspondence: Lev Tarasov (lev@mun.ca)



Abstract. We present an ensemble of Last Glacial Inception (LGI) simulations for the Northern Hemisphere that largely captures inferred ice volume changes within proxy uncertainties. This ensemble was performed with LCice 1.0, a coupled ice sheet and climate model, varying parameters of both climate and ice sheet components, as well as the coupling between them. Certain characteristics of the spatio-temporal pattern of ice growth and subsequent retreat in both North America (NA) and Eurasia (EA) are sensitive to parameter changes, especially with respect to regional rates of ice growth and retreat. We find that the initial inception of ice over NA and EA is best characterized by the nucleation of ice at high latitude and high elevation sites. Subsequent spreading and merger along with large-scale conversion of snow fields dominate in different sectors. The latter plays an important role in the merging of eastern and western ice regions in NA.

The inception peak ice volume in the ensemble occurs approximately at 111 ka and therefore lags the summer 60°N insolation minimum by more than 3 kyr. Ice volumes consistently peak earlier over EA than NA. The inception peak in North America is characterized by a merged Laurentide and Cordilleran ice sheet, with Davis Strait covered in ice in ~80% of simulations. Ice also bridges Greenland and Iceland in all runs by 114 ka and therefore blocks Denmark Strait. This latter feature would thereby divert the East Greenland Current and Denmark Strait overflow and thereby potentially have a significant impact on ocean circulation. The Eurasian ice sheet at its inception peak varies across ensemble runs between a continuous ice sheet to multiple smaller ice caps.

In both continents, the colder high latitudes (Ellsmere and Svalbard) tend to grow ice through the entire simulation (to 102 ka), while lower latitudes lose ice after ~110 ka. We find temperature decreases over the initial phases of the inception lead to the expansion of NA ice sheet area, and that subsequent precipitation increases contribute to its thickening. EA ice sheet area also expands with decreasing temperatures, but sea ice limits any increases in precipitation, leading to an earlier retreat away from the EA maximum ice sheet volume.

We also examine the extent to which the capture of both LGI ice growth and retreat constrains the coupled ice/climate model sensitivity to changing atmospheric pCO₂. For a standard transient climate response experiment (1% increase in pCO₂ until doubled), warming ranges between 0.6-2.0°C for our initial set of 500 simulations without LGI constraint. The warming is reduced to 0.7-1.4°C for the 55 member ensemble that captures both LGI ice growth and retreat. This therefore underlines the potential value of fully coupled ice/climate modelling of last glacial inception to constrain future climate change.



1 Introduction

Reconstructions of sea level change from corals and oxygen isotope records (*e.g.* Waelbroeck et al., 2002; Siddall et al., 2003) along with some limited inferences from glacial geology (Clark et al., 1993) indicate that between about 120 and 115 ka, large ice sheets formed rapidly in the Northern Hemisphere (NH). By 110 ka, mean sea level is inferred to have been approximately 30 45-65 m lower than present (Lambeck and Chappell, 2001; Waelbroeck et al., 2002; Siddall et al., 2003; Lisiecki and Raymo, 2005) or about half of that inferred for LGM. Contrary to the common perception that ice sheet growth is a much slower process than ice sheet retreat, this large last glacial inception (LGI) growth in ice volume occurred over approximately the same duration (~ 10 kyr) as the last deglaciation. This rapid ice sheet growth was subsequently followed by ice retreat for the next 10 kyr (Bard et al., 1990; Chappell et al., 1996; Gallup et al., 2002).

35 However, aside from global constraints on sea level, little is known about the LGI evolution of individual ice sheets. The terrestrial geological record was largely destroyed by subsequent ice advance and retreat, and any proxy records that may have survived are scattered and have large age uncertainties (Andrews and Barry, 1978; Lambeck and Chappell, 2001; Stokes et al., 2012). This uncertainty percolates into the associated changes in the climate system (especially over terrestrial sectors) both due to similar limitations in proxy records for climate characteristics and uncertainties in the required ice sheet boundary 40 conditions for running climate models over this interval.

Given the rapidity of LGI sea level decreases and the relative sizes of last glacial maximum ice sheets, it is generally assumed that North America contributed a significant fraction to this sea level fall. The rapidity of ice growth has motivated the development of one hypothesis to characterize glacial inception over North America: widespread thickening of snowfields (Andrews and Mahaffy, 1976). A second complementary hypothesis stems from consideration of where present-day lower lat- 45 titude glaciers exist and posits ice sheet spreading from high elevation nucleation sites (Weertman, 1964). A previous attempt to simulate the inferred sea level drop during LGI supported the widespread snowfield thickening paradigm (Calov et al., 2005a). The model used in that study employed very low resolution (51° longitude by 10° latitude for atmosphere and approximately 100 km for the ice sheet model). Only 3 transient simulations were presented. Given the uncertainties in the proxy data and models, a much larger ensemble of simulations that better captures model uncertainties is required to assess how representative 50 this result is of the actual growth of ice sheets during the LGI.

Ideally, model studies of LGI would employ sophisticated Earth System Models (ESMs) at high resolution bidirectionally coupled to ice sheet models to produce ensembles of transient experiments that span the uncertainties of the relevant data and processes, but this is computationally too expensive. Instead, model studies of LGI tend to make one of two simplifications. First, general circulation model- (GCM) based studies treat the climate in a sophisticated way, but rely on a small number of 55 snapshot experiments without interactive ice sheets. Ice sheet boundary conditions are prescribed which can lead to a modelled climate that is inconsistent with the prescribed ice extent (Pollard and PMIP-participating groups, 2000). Furthermore, the reliance of these studies on at most a few model runs severely limits any possible uncertainty assessment. Second, experiments performed with ice sheet and climate models coupled together tend to employ Earth System Models of Intermediate Complexity (EMICs). These model configurations include interactive ice sheets and can be run with transient boundary conditions.



60 However, their low climate model resolution means more processes must be highly parameterized, and some key ice/climate feedbacks are not modelled at all.

Due to such simplifications, most LGI model studies have been unable to simultaneously simulate the required rapid ice build-up until around 110 ka with the subsequent retreat (*e.g.* Tarasov and Peltier, 1997a; Calov et al., 2009). Prior to the development of the LCice 1.0 (Bahadory and Tarasov, 2018), the one coupled ice/climate modelling study that adequately
65 captured both the growth and retreat phases of LGI required the use of an imposed (albeit plausible) aeolian dust deposition forcing and temperature bias correction (Ganopolski et al., 2010). A further limitation in this latter study is that the CLIMBER EMIC employed uses a 2.5D statistical-dynamical atmospheric model with very limited longitudinal resolution (51.4°) and a 3 basin 2D ocean model¹.

Temperature bias corrections are ubiquitous in coupled ice sheet and climate modelling, relying on the standard (though
70 often implicit) justification that climate models are more likely to better capture the perturbative response to radiative forcing changes than the actual present-day temperature distribution. This comes with the trade-off that the bias correction is generally not imposed internally in the climate model and therefore the glacial climate imposed on the ice sheet model is dynamical self-inconsistent.

LCice 1.0 is so far the only fully coupled ice sheet-climate model capable of simulating both the rapid growth and retreat
75 phase of the LGI (Bahadory and Tarasov, 2018) without using any bias correction or imposed dust forcing. It includes the main feedbacks between the ice sheet and the atmosphere and ocean, many of which have not been resolved in previous coupled EMIC/ice sheet modelling studies (Bahadory and Tarasov, 2018). LCice 1.0 is also fast enough to generate ensembles of glacial cycle timescale transient simulations.

Thus, we employ LCice 1.0 in this study to generate an ensemble of transient LGI simulations to address the following ques-
80 tions. How did each ice sheet most likely evolve through its inception phase, and which of the two aforementioned paradigms best describes this evolution? More fundamentally, is the spatio-temporal pattern of LGI a single attractor in the phase space of possible inceptions, or could small changes in initial conditions or physical properties (*e.g.* snow albedo) lead to a significantly different pattern (more crudely, did the LGI have to happen the way it did)? This question includes an examination of the extent to which the evolution of ice sheets in Eurasia (EA) and North America (NA) are correlated. Expanding this phase space
85 analysis to the climate, we also examine how the climate conditions (insolation, carbon dioxide, temperature and precipitation) facilitate or hinder the rapidity of ice growth and retreat.

The capture of LGI ice growth and subsequent decay presumably constrains the sensitivity of the coupled ice and climate model. As the largest sources of uncertainty in the coupled model are the internal feedbacks and not the much more tightly constrained direct radiative forcing of changing atmospheric $p\text{CO}_2$, LGI offers a potential constraint on ice/climate model
90 sensitivity to the projected increases in atmospheric $p\text{CO}_2$ our planet is facing. We therefore also examine the extent to which capturing the LGI constrains the Transient Climate Response (TCR) of the coupled model to doubling atmospheric $p\text{CO}_2$.

¹On other hand, it should be noted that the relative quality of modelled LGM ice extent in Ganopolski et al. (2010) attests the potential value of using fast EMICS like CLIMBER



In section 2, we first review LCice 1.0 and its components, and the choice of our parameters for the ensemble study. We discuss the phasing of LGI in our ensemble in section 3 in terms of ice sheet and climate evolution. The implications of our results for ice/climate model sensitivity are discussed in section 2.3.

95 2 Experimental setup

We ran an ensemble of 500 simulations for the North American, Greenland and Eurasian ice sheets using the coupled model LCice 1.0. These 500 simulations were previously sieved from a larger ensemble of 2000 simulations covering the preindustrial to present day interval. Only 55 out of 500 inception simulations could approximately replicate the pattern of sea level lowering due to ice sheet build up, followed by sea level increase, as suggested by reconstructed proxies of Waelbroeck et al. (2002);
100 Lisiecki and Raymo (2005).

In detail, the acceptance criteria for the 55 “acceptable” simulations were: 1) at least a 30 m eustatic sea level contribution to the LGI sea level minimum and 2) at least a 10% subsequent increase in eustatic sea level by 105 ka. The rejected simulations generally underestimated total ice volume, though a small number of simulations captured appropriate growth without a subsequent retreat phase. For the rest of this paper, the term “ensemble” refers to this sieved group of 55 simulations.

105 2.1 Ensemble parameters and sensitivity analysis

The ensemble is constructed by varying 18 parameters, 5 of which are found in LOVECLIM, 9 in the GSM, and 4 in the coupler, as described in (Bahadory and Tarasov, 2018). The LOVECLIM ensemble parameters include snow albedo, bare-ice albedo, melting ice albedo, the humidity threshold for parameterized precipitation, and the cloud parameterization scheme. The GSM ensemble parameters address uncertainties in basal drag, ice calving, sub-shelf melt, and deep geothermal heat flux.
110 Ensemble parameters related to the coupling procedure include spinup length and start time, upscaling method, and the method used to calculate the vertical temperature gradient. Each ensemble parameter and associated sensitivity analysis for the coupled model is described in detail in Bahadory and Tarasov (2018).

2.2 Initial conditions and spin-up

Since the extent of the Greenland ice sheet during the Eemian is not well constrained, the initial state of the ice sheet at the
115 start of all simulations is set to its present-day configuration. Future work will use an initialization from ongoing Greenland ice sheet model calibration. The initial climatic state is provided by a 3 to 5 kyr LOVECLIM spinup under transient orbital and greenhouse gas forcing from the previous interglacial, with present-day topography and ice mask provided as boundary conditions.

2.3 Transient climate response experiment

120 Initial conditions for the TCR simulations are generated by running the model for different lengths of time to year 1850CE, as specified by the spinup component of the parameter vector (between 3 and 5 kyr). Both the orbital parameters and GHG



vary during the spinup. Following the IPCC AR5 protocol, our Transient Climate Response (TCR) ensemble starts at 1850 CE (with year-appropriate GHG and orbital forcing). Atmospheric pCO₂ increases by 1% every year until reaching a concentration twice that of pre-industrial after 70 years.

125 2.4 Models

2.4.1 LOVECLIM

LOVECLIM is a coupled EMIC, consisting of a quasi-geostrophic atmosphere (ECBilt), a primitive equation ocean with dynamic sea ice (CLIO) and dynamic vegetation (VECODE). The spatial resolution of the atmospheric component is T21. The ocean and sea ice components each have a resolution of 3°. LOVECLIM is fast enough to simulate LGI (120 ka to 100 ka) in
130 less than 3 weeks using a single commodity core. It has therefore been used to simulate a wide range of different climates from the LGM (Roche et al., 2007) through the Holocene (Renssen et al., 2009) and the last millennium (Goosse et al., 2005) to the future (Goosse et al., 2007).

Interpretation of model-based results always requires cognizance of model limitations. Aside from the simplified atmospheric dynamics and low grid resolution, a key limitation of LOVECLIM for our study is the fixed land-ocean mask. With an
135 inferred LGI maximum sea level drop of approximately 45-65 m, throughflow through ocean gateways can change significantly (including complete closure of Bering Strait). LOVECLIM is unable to handle a changing land mask, except for the Bering Strait, where throughflow is parameterized as a function of modelled sea level and regional ice sheet cover. Other potentially important factors which can affect the results include simplified radiation and hydrology schemes, and missing feedbacks of dust on radiative forcing.

140 2.4.2 GSM

The glacial systems model (GSM) is built around a thermo-mechanically coupled ice sheet model. It includes a 4 km deep permafrost-resolving bed thermal model (Tarasov and Peltier, 2007), fast surface drainage and lake solver (Tarasov and Peltier, 2006), visco-elastic bedrock deformation (Tarasov and Peltier, 1997b), Positive Degree Day surface mass balance with temperature dependent degree-day coefficients derived from energy balance modelling results (Tarasov and Peltier, 2002), sub-grid
145 ice flow and surface mass balance for grid cells with incomplete ice cover (Morzadec and Tarasov, 2017), and various ice calving schemes for both marine and pro-glacial lake contexts (Tarasov et al., 2012). For the results herein, ice shelves are treated using a crude shallow ice approximation with fast sliding. The GSM runs at 0.5°longitude by 0.25°latitude grid resolution.

2.4.3 LCice 1.0 coupler

The LCice coupler is designed to extract, regrid, and exchange the required fields between atmosphere and ocean components
150 of LOVECLIM and the GSM asynchronously (*i.e.* LOVECLIM and the GSM are run sequentially with boundary conditions from the other model fixed between data exchanges). The time between data exchanges was chosen to be 20 years as the



optimal balance in sensitivity tests between efficiency and proximity to shorter coupling time step solutions (Bahadory and Tarasov, 2018).

Fields passed from the ice sheet to the atmosphere include ice mask and surface elevation, the latter via one of the three included schemes (simple, envelope, and silhouette, the choice of which is under ensemble parameter control). The atmosphere to ice coupling includes the monthly mean and standard deviation temperature and monthly mean precipitation, evaporation, wind direction and magnitude, and vertical temperature lapse-rate. LCice 1.0 uses an innovative scheme to downscale precipitation to the ice model grid that accounts for orographic forcing on the GSM grid resolution topography. Temperature downscaling uses the evolving vertical surface temperature gradient field of LOVECLIM. The coupler also includes a simple radiative cloud parameterization to compensate for the present-day prescribed radiative cloud cover of LOVECLIM.

In ice sheet-ocean interactions, the GSM determines the runoff routing, and passes freshwater fluxes to the ocean model, while the ocean model provides the GSM with vertical temperature profiles, required to calculate sub-shelf melt. Details of each component of the coupling and their influence are described in Bahadory and Tarasov (2018).

Given model limitations, there is no one best run in the ensemble. Instead, different runs have different features, each of which will likely have different patterns of misfits against inferred proxy records. In the following results, we crudely interpret feature frequency in the ensemble to be a partial metric of feature likelihood, though this is far from a rigorous probabilistic analysis.

3 Results

The LCice 1.0 ensemble reproduces the reconstructed pattern of rapid ice sheet volume growth and retreat during the LGI in 55 of the 500 runs. The total Northern Hemisphere ice volume averaged over the ensemble of 55 runs is plotted in figure 1. No single ensemble parameter determines which runs meet the filter condition (not shown).

The maximum ice volume achieved by the LCice 1.0 ensemble during inception is lower than that inferred by Lisiecki and Raymo (2005), but within the collective uncertainty of the three reconstructions presented here (Waelbroeck et al., 2002; Siddall et al., 2003; Lisiecki and Raymo, 2005). The ensemble mean maximum ice volume is about 5 m in sea level equivalent (SLE) short of the Red Sea record (Siddall et al., 2003, dark purple in figure 1). This under-estimation is likely due in part to the absence of any contribution from the Antarctic ice sheet (and perhaps Patagonian and Tibetan ice caps). This under-estimation is also consistent with the fact that the simulated ice sheet volumes never reach the peak rate of ice growth indicated by any of the sea level reconstructions.

The timing of when the LCice 1.0 simulations achieve their maximum inception ice sheet volume is bounded by the three proxy-based reconstructions shown in figure 1. All but the Greenland ice sheets reach their maximum LGI ice volumes at least 3 kyr after the 60°N summer insolation minimum (orange line in figure 1). The earliest retreat occurs in the Red Sea reconstruction. This reconstruction suggests a faster decrease in pre-stadial sea level compared to that of the other three records, and its timing of the sea level minimum and subsequent sea level rise is slightly advanced of the LCice ensemble mean. The LCice maximum ice sheet volume occurs approximately midway between the timing of minimum insolation at 60°N and

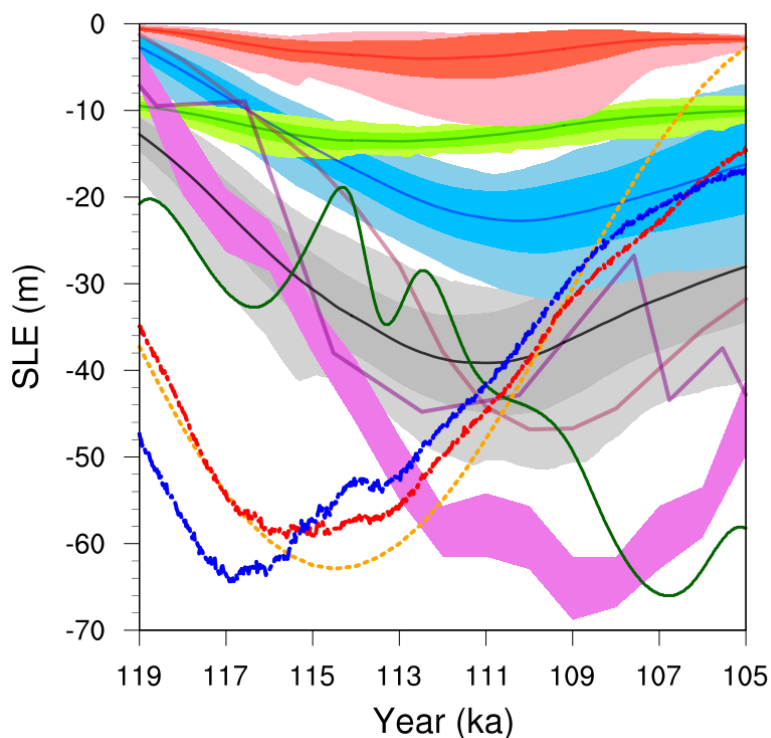


Figure 1. The time evolution of total (black), NA (blue), EA (red), and Greenland (green) ensemble mean ice volumes in m sea level equivalent (SLE) between 119 and 105 ka. The dark shading indicates the ± 1 standard deviation range around the mean. The light shading shows the range between minimum and maximum ice volumes in the ensemble. The purple area, light purple, and dark purple lines show the respective proxy-based sea level reconstructions from Lisiecki and Raymo (2005) with 1 sigma, Waelbroeck et al. (2002), and Siddall et al. (2003). The orange and dark green lines depicts the timing of insolation changes at 60°N and $p\text{CO}_2$, respectively. The JJA ensemble mean temperatures over 50°N - 65°N of NA and 60°N - 75°N of EA are shown as thick-dotted blue and red lines, respectively.

185 minimum $p\text{CO}_2$. The Lisiecki and Raymo (2005) stadial peak occurs 2 kyr later, approximately halfway between the 60°N JJA
(mean June July August) orbital minimum at 114.5 ka and the subsequent maximum at 104 ka.

A second test of the representativeness of these simulations for the LGI is made between temperature changes from a
glaciological inversion of the GRIP ice core $\delta^{18}\text{O}$ record (Dansgaard et al., 1993; Tarasov and Peltier, 2003) and annual-mean
temperatures calculated from the model grid cell containing its location. The ensemble mean 2m temperature anomaly relative
190 to 119 ka follows the general trend of GRIP reconstructed temperatures in figure 2 until ~ 112 ka. Individual runs have higher
decadal to centennial scale variance than that of the GRIP record. However, the large millennial scale variability of the GRIP
record inversion is not captured by the simulations. The ensemble-mean annual temperatures from the GRIP site subsequently
diverge from reconstructed temperatures after approximately 111 ka. At this time, simulated temperatures increase at the

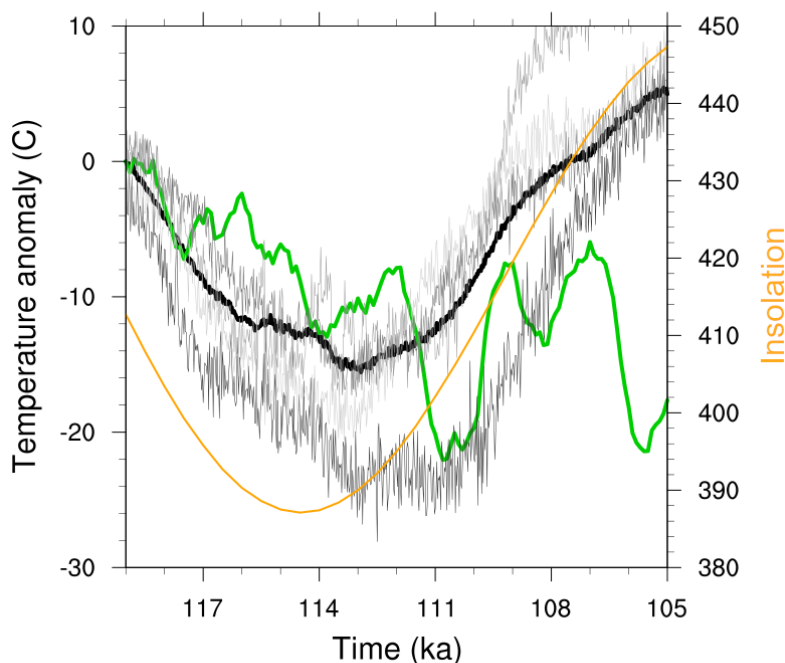


Figure 2. Annual mean 2 m temperature anomaly relative to 119 ka for the GRIP ice-core (green) (Dansgaard et al., 1993; Tarasov and Peltier, 2003), ensemble mean (thick black), and three individual runs (gray lines). The orange line depicts the timing of insolation changes at 60°N.

GRIP site following insolation changes, whereas there is no evidence of a similar increase in the GRIP record temperature
195 inversion. Instead, reconstructed GRIP temperatures exhibit multi-millennial timescale oscillations around stable, stadial (cold
state) temperatures. It is unclear what mechanism would sustain stadial temperatures over central Greenland under increasing
insolation, especially since the simulations consistently predict that strong warming should result. It may be this discrepancy
reflects in part a lack of accounting for at least two standard sources of uncertainty in water isotope to temperature inversions:
changes in the moisture source region and changes in the seasonal distribution of precipitation.

200 3.1 Glacial inception phase-space

Having established that LCice 1.0 is able to capture both the ice sheet growth and retreat phases of the LGI, we explore the
pattern(s) of the ice growth and retreat across ensemble members. We start by analyzing the spatial patterns of EA and NA ice
sheets at two diagnostic time intervals: first, the early stage of ice build up, and second, during the peak of the inception around

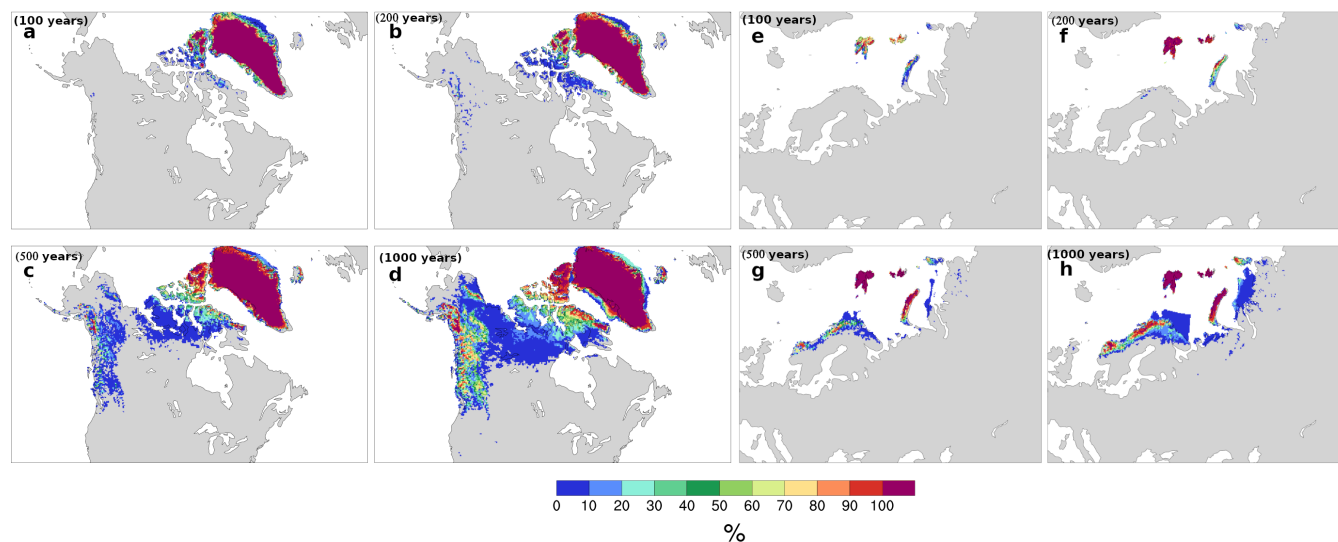


Figure 3. **Left.** Percent of runs exhibiting ice cover in each grid cell for NA after **a** 100, **b** 200, **c** 500, and **d** 1000 years of simulation. **Right.** Percent of runs exhibiting ice cover in each grid cell for EA after **e** 100, **f** 200, **g** 500, and **h** 1000 years of simulation.

112 ka. Next, we explore the consistency of ice and climate evolution between these two intervals and during the subsequent
205 retreat phase.

3.1.1 Spatial pattern of first appearance of ice

Despite having different start times (due to different calendar start years between 122 ka and 119 ka and spinup lengths varying
between 3 to 5 kyr), all simulations start growing ice in the first 100 years of simulation (figure 3.a). Therefore, we analyze the
spatial patterns of the first appearance of ice in the first 1000 years of simulation, rather than aggregating simulations according
210 to a common calendar year.

In NA, all runs have extensive glaciation over Ellesmere and eastern Devon Island after 100 years of transient simulation
(figure 3). Subsequently, ice starts to spread through the Arctic archipelago and Baffin Bay sector of Baffin Island. This is in
agreement with past suggestions that the first ice nucleation in NA occurs over the Canadian Archipelago with further growth,
merger, and then expansion to southern and western regions (Weertman, 1964). This result is also consistent with the ongoing
215 presence of extensive glaciers and small ice caps in this region.

By 1000 years, more than 20% of runs have extensive ice over the Pacific Cordillera down to 48°N. Northwestern Alaska
remains ice free for the first 1000 years in all runs as does the non-Cordilleran sector of NA below 61°N.

To get a more detailed sense of what glacial inception might look like, it is worth examining ice sheet evolution for one of
the best fitting runs (to sea level proxies). By 119 ka, most of NA above 65°N has ice cover, though much of it with surface
220 elevation less than 500 masl (figure 4). The Canadian Cordilleran at this time has near complete ice coverage with all surface
elevation above 1000 masl.

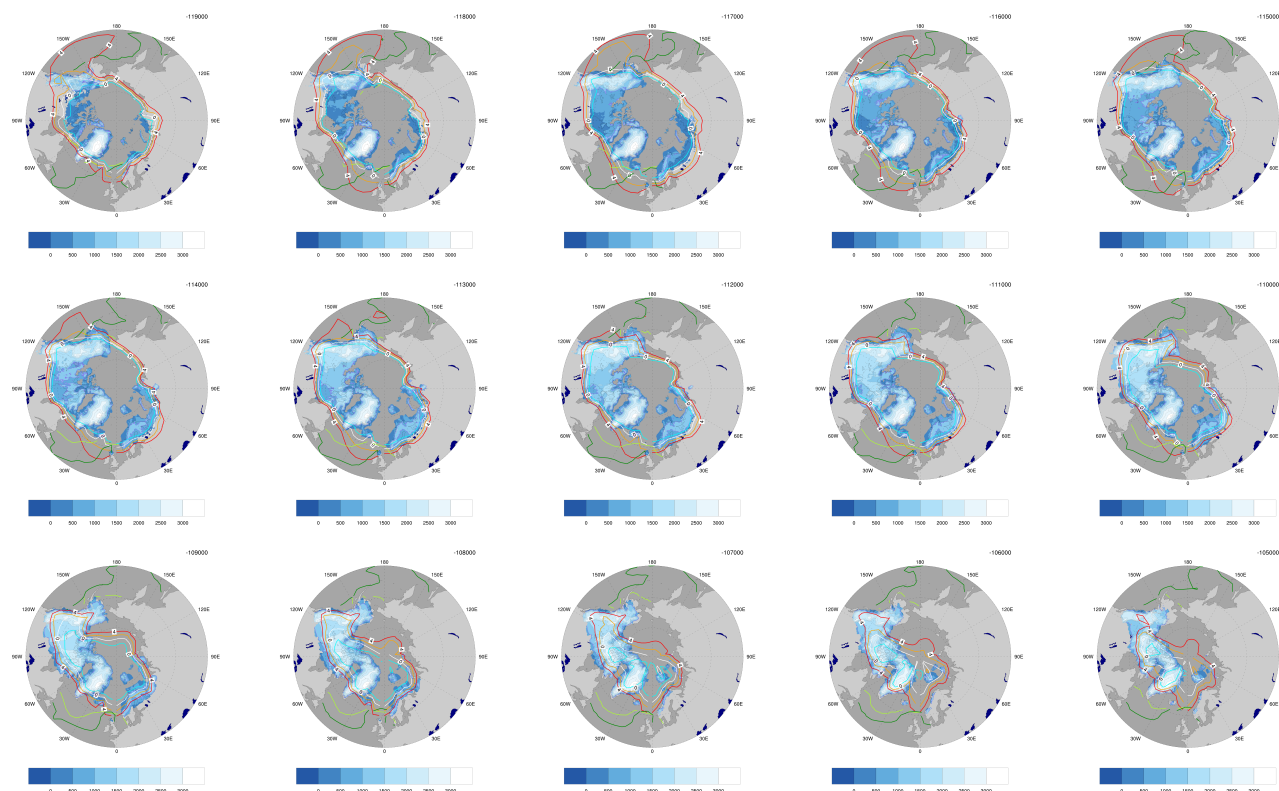


Figure 4. The evolution of ice sheet elevation (shaded areas in light blue-white gradient), 2 meter JJA temperature (-2°C to 4°C), and sea ice seasonal maximum and minimum extent (dark and light green) for every 1 kyr from 119 ka to 105 ka for one of the best fitting (to proxy sea level records) simulations of the ensemble. The 1000 m elevation contour is in purple.

Ice growth over EA begins over Svalbard within the first 100 years of simulation in all runs, with some runs also showing ice cover over other islands in the region (figure 3.e and f). After 200 years, Svalbard and Franz Joseph Land have complete ice cover in almost all runs, while Fennoscandia has no ice in almost all runs. By 500 years, much of Novaya Zemlya has ice cover in almost all runs. Ice nucleation over Fennoscandia starts over the high precipitation and higher elevation Norwegian and Barents Sea sectors for most runs within 1000 years. Fewer than 10% of runs have any ice over Continental Russia during the first 1000 years.

Note that in figures 3.e-h, parts of the Fennoscandia ice margins in the Barents Sea follow unphysical, straight lines. This is an artifact of the model setup for submarine melt and is discussed in more detail in the Discussion.

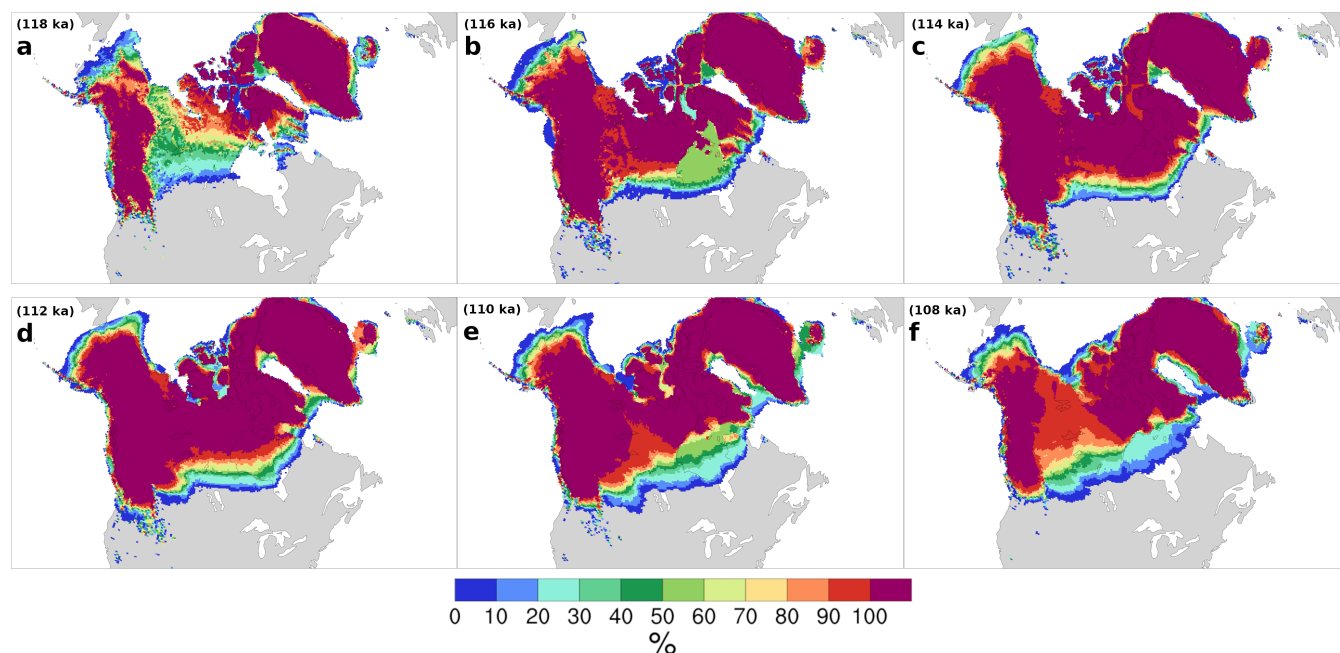


Figure 5. NA ice extent ensemble probability distribution at **a** 118 ka, **b** 116 ka, **c** 114 ka, **d** 112 ka, **e** 110 ka, and **f** 108 ka. The 118 ka and 116 ka are included to provide the history before the peak and are not discussed.

230 3.1.2 Spatial pattern of the Last Glacial Inception maximum ice

To capture the maximum in ice volume for EA and NA during the LGI, we consider time slices for 114 ka, 112 ka, 110 ka and 108 ka in figures 5 and 6. We aggregate our simulation results according to their boundary condition years rather than their simulation years.

At 114 ka, the Cordilleran is completely ice covered in all runs down to approximately 45°N. Central NA ice extends to
235 approximately 55°N until a sharp northward turn of the southern ice margin over James Bay extending to the east (figure 5). The Greenland and Iceland ice sheets are bridged by ice across Denmark Strait in all runs by 114 ka (with most runs having grounded ice right across the Strait). Also, Alaska is almost fully ice-covered in all of the simulations, while Labrador and eastern NA remains ice-free, likely due to warm model biases in this region.

The main differences in peak LGI NA ice extent between ensemble members occur: at the northwestern Alaskan ice margin
240 (40% of ensemble runs cover Bering Strait at 114 ka), at the southern margin, and over Davis Strait. For the latter, approximately 80% of simulations create an ice bridge connecting the Laurentide and Greenland ice sheets across the Strait. This ice bridge generally starts out from a merger of opposing ice shelves. For some (but not all) ensemble runs, it can also ground right across the Strait and therefore isolate Baffin Bay from the Labrador Sea.

After the stadial peak in NA ice volume, the main variation between ensemble members appears in the rate of ice retreat. Ini-
245 tially, while the south-eastern ice margin rapidly retreats to higher latitudes in simulations with smaller ice sheets, simulations

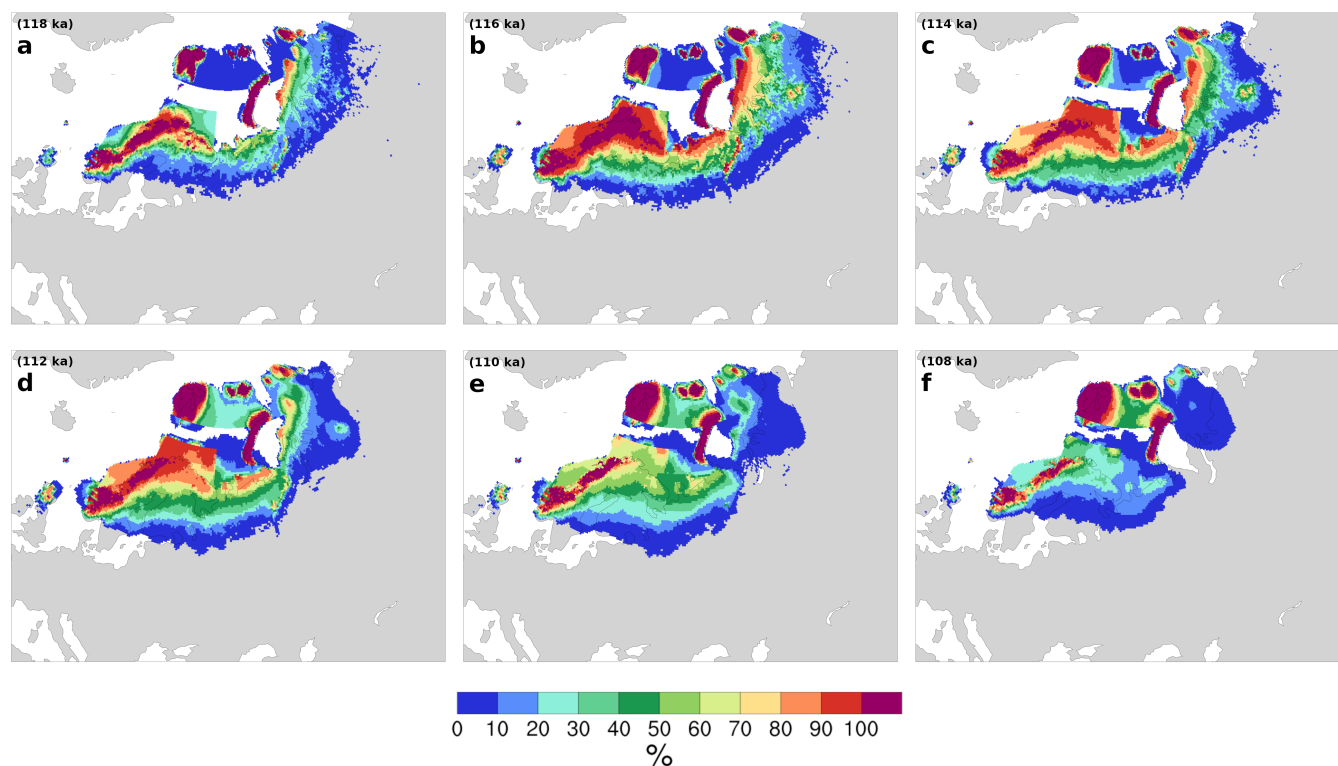


Figure 6. EA ice extent ensemble probability distribution at **a** 118 ka, **b** 116 ka, **c** 114 ka, **d** 112 ka, **e** 110 ka, and **f** 108 ka. The 118 ka and 116 ka are included to provide the history before the peak and are not discussed.

with larger ice sheets show little change in ice extent. This difference in behaviour leads to the largest difference in ice extent over Hudson Bay at 110 ka, when the entire area is covered by approximately 20% of the simulations and 30% are ice-free in this region. By 108 ka, the Laurentide and Cordilleran ice sheets are separated in only 10% of the simulations, fewer than 20% of runs simulate a connected Greenland-Iceland ice sheet, and the ice bridge across Davis Strait remains in fewer than 10% of runs.

A key feature from the sample best run snapshots (figure 4) is the continuous slow thickening of Ellesmere Island ice right through to 105 ka. Thus, limited snow accumulation appears to be the major controlling climate factor for this region during LGI. The ice dome north of Hudson Bay also only attains its maximum elevation at 107 ka.

Similar to the early phases of the inception, ice extent over EA is more variable between ensemble members around the stadal peak time (116 ka to 112 ka) compared to NA (figure 6). The maximum area of 100% cross-ensemble continental ice cover occurs at 116 ka, with a significant reduction by 114 ka. Fewer than 10% of runs increase their southern ice extent through to 112 ka. Scotland exhibits some ice cover in the majority of runs, but the North Sea remains ice-free.

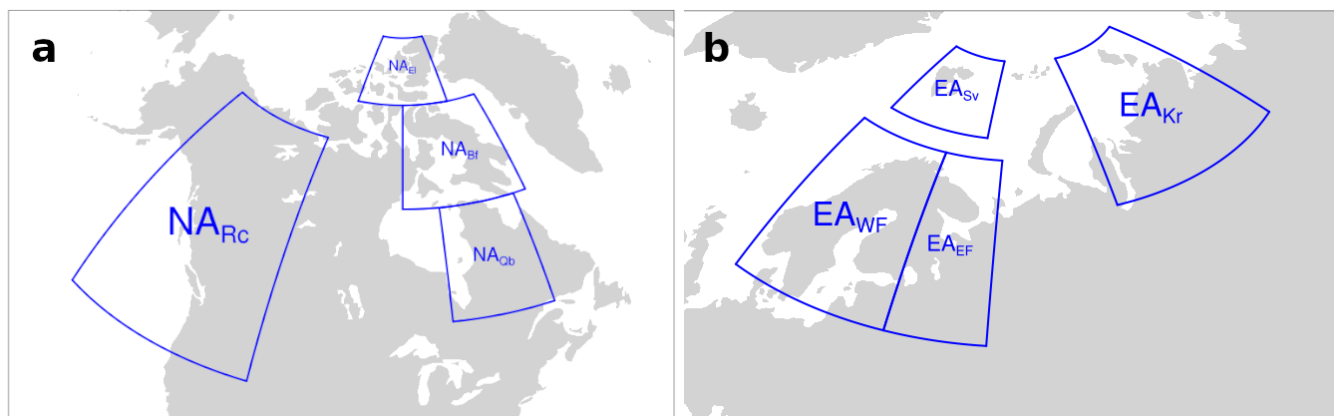


Figure 7. a. NA sectors, and b. EA sectors

3.2 Temporal pattern of ice evolution across the ensemble

As shown in the previous section, the rates of ice growth and retreat are not consistent through the LGI in all regions, especially in EA. To diagnose the development of these ensemble member differences in time, we subdivide NA and EA into four sectors each (outlined in figure 7) and examine the evolution with time of ice volume in each sector along with correlations between sector maximum ice volumes.

The NA sectors include the Canadian Archipelago separated into Ellesmere Island (NA_{El}), Baffin Island (NA_{Bf}), Quebec (NA_{Qb}), and the Rockies (NA_{Rc}). The EA sectors include the north-western Barents Sea and Svalbard (EA_{Sv}), the Kara Sea and nearby land (EA_{Kr}), and eastern and western Fennoscandia (EA_{EF} and EA_{WF}).

3.2.1 North American ice sheet

In all NA regions in figure 8 except NA_{El} , ice volume increases to a maximum sometime between 112 ka and 109 ka and then decreases. In NA_{El} , the coldest region of NA, ice volume increases throughout the LGI in most simulations.

Generally, the ice sheet growth phase for each sector is more consistent between runs than its retreat phase. In sector NA_{Bf} (figure 8b), ~10% of simulations lose between 1 and 1.5 m SLE of ice between 112 and 107 ka and maintain a constant ice volume afterwards. The rest of the runs show a range of behaviours, from almost no ice loss to 80% loss. In contrast, in NA_{Qb} , the most southern and warmest sector, the maximum ice volume varies between almost zero to more than 1 m SLE, and no simulation sustains ice cover through to 102 ka. The NA_{Rc} region spans the widest range of latitudes, but it also contains some of the highest-elevation sites of NA. It shows both strong ice growth and a wide range of ice loss scenarios over the LGI. Notably, ice develops over western NA (NA_{Rc}) at the same time as it is growing in the east.

One pattern that emerges most strongly in NA_{Qb} is that the runs with larger ice sheets tend to have delayed peak times. This is consistent with the observation in the previous section that runs with the largest NA ice sheet extent retreat more slowly than those with smaller ice sheets.

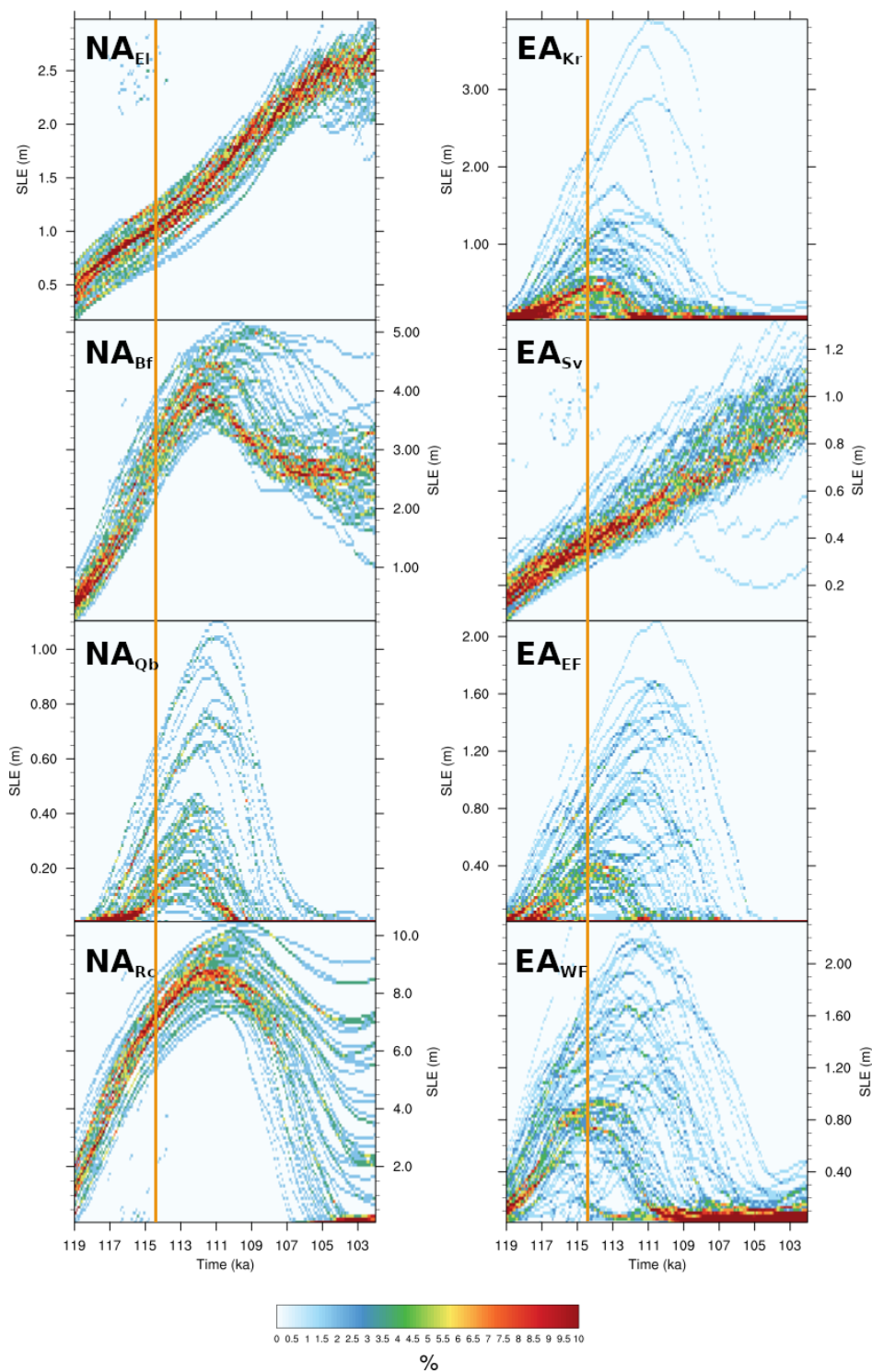


Figure 8. Left. NA ensemble distribution of ice volume during LGI in NA_{EI} , NA_{Bf} , NA_{Qb} , and NA_{Rc} . Right. EA ensemble distribution of ice volume during LGI in EA_{Kr} , EA_{Sv} , EA_{EF} , and EA_{WF} . The vertical orange line shows the timing of the minimum summer insolation at $60^{\circ}N$.



3.2.2 Eurasian ice sheet

280 In EA, the most northern (and coldest) sector, EA_{Sv} has steadily increasing ice volume throughout the LGI. This pattern is
similar to that observed for NA_{El} . Otherwise, the rest of EA sectors show ice growth and retreat patterns similar to NA_{Qb} ,
where there is a wide variation in the total ice volume reached and (near-) complete ice loss by the end of the LGI. These
regions also generally reproduce the tendency for larger ice sheets to have later peak ice volumes, ranging between 114 and
110 ka. However, in EA_{EF} and EA_{WF} there are some notable exceptions to this pattern, where some simulations exhibit late
285 peak times (ca 108ka) for a wide range of maximum ice volumes.

3.3 Relationships between changes in the North American and Eurasian ice sheets

We have examined the build-up and retreat of ice sheets in NA and EA independently. Past modelling studies indicate that
the presence of NA ice can affect conditions over EA (Beghin et al., 2013; Colleoni et al., 2016; Liakka et al., 2016; Ullman
et al., 2014; Kageyama and Valdes, 2000) and therefore potentially EA evolution. Thus, we consider next whether there is any
290 evidence for such a relationship acting in this ensemble.

Comparisons of EA maximum ice volume versus NA maximum ice volume in figure 9 indicate that there exists no simple
relationship between these two fields. Small NA ice volumes correspond to small EA ice volumes. However, when NA ice
volumes are larger, figure 9 suggests a possible bifurcation in the runs.

Although there is no simple relationship between the volumes of the NA and EA ice sheets, there is a relationship between
295 the timing of the peak ice volume for these two ice sheets in most ensemble members. In figure 10a, the peak ice volume and
peak ice area nearly always occurs earlier in EA than in NA. This result is expected given the smaller size and related stronger
sensitivity of the EA ice sheet to orbital forcing. The duration of this lead depends strongly on model parameters and ranges
between 200 years to 6 kyr. In a small subset of runs, the EA ice volume peaks early (~ 115 ka) or late (~ 110 ka) regardless of
the timing of the NA ice volume peak (further evidence in support of the aforementioned possible bifurcation).

300 The correlation in the timing that maximum ice volumes are reached in NA and EA in most runs in figure 10a may indicate
that these ice sheets are affecting each other's growth and retreat, or it may indicate that the parameter choices that lead to
larger ice sheets in one region also encourage growth in the other. One plausible mechanism whereby the NA ice sheet may
affect the development of the EA ice sheet is through a reduction in hemispheric temperatures. However, there is no evidence
of this, as the timing of maximum EA ice volume (figure 10b) has no consistent phase relationship with the timing of EA
305 minimum temperature.

3.4 Climate of the Inception

Having documented the phase space of ice sheet changes and identified the more robust features in our ensemble of LGI
simulations, we now consider relevant controls from the climate system. To that end, we focus on temperature and precipitation
as the two main controls on ice sheet thickness and extent (at least for terrestrial components). These are in turn affected by
310 Northern Hemisphere sea ice extent (which alters the exchange of heat and moisture between the atmosphere and ocean), the

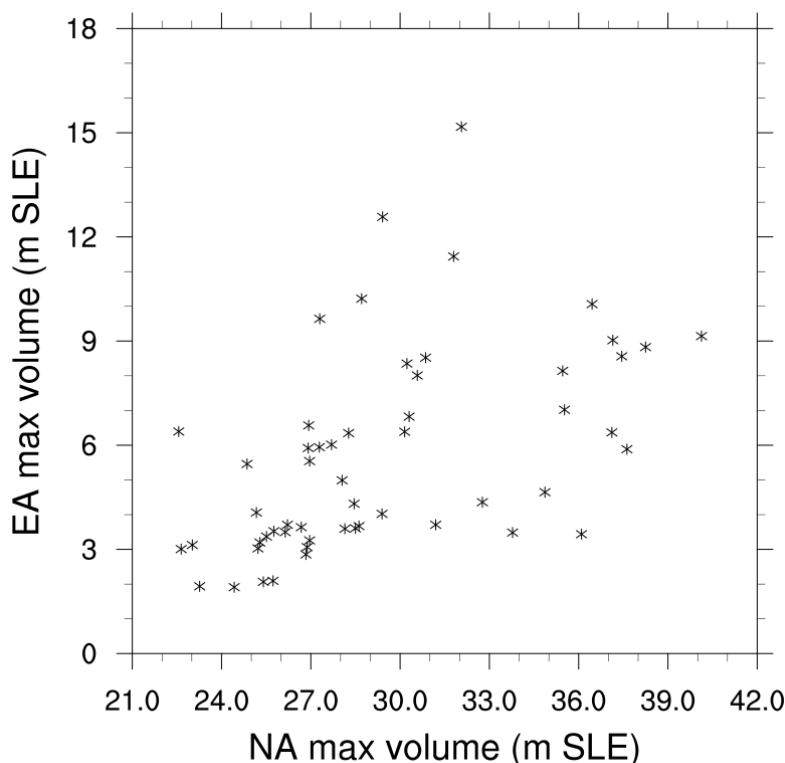


Figure 9. The maximum volume of the NA and EA ice sheets for individual runs.

AMOC (through changes to oceanic heat transport to high latitudes), and the latitude of the jet stream (through changes to atmospheric heat transport and the location of storm tracks).

Northern summertime temperature and annual precipitation are ice-sheet relevant climate characteristics that most directly control ice sheet extent and thickness. For our ensemble, both temperature and precipitation of NA and EA (figure 11) show abrupt reductions early in the LGI interval initially in phase with the reduction in insolation at 60°N. In NA, summer temperature and annual precipitation reach their respective minimum values at 116.8 and 116.1 ka, approximately 2.3 and 1.6 kyr earlier than insolation. An increase in the radiative forcing from changing atmospheric pCO₂ (purple time series in 11) after 116.2 ka and especially a subsequent decrease after 114.3 ka approximately correspond with the interval of discrepant NA mean summer temperature change (relative to insolation forcing). Since the relatively high albedo ice sheets and sea ice tend to be fairly extensive by this time (figures 5, 6 and 11), changing insolation will also be a smaller contributor to the regional energy balance. The possible role of changes in AMOC and sea ice cover are examined below.

The early stages of ice growth in NA appear to be dominated by ice sheet expansion in response to regional cooling, since precipitation is decreasing. In 119 to 117 ka snapshots of near-surface temperature and ice sheet elevation from a single simulation in figure 4, the southern ice sheet margins tend to be located between the -2°C to 0°C JJA isotherms in most

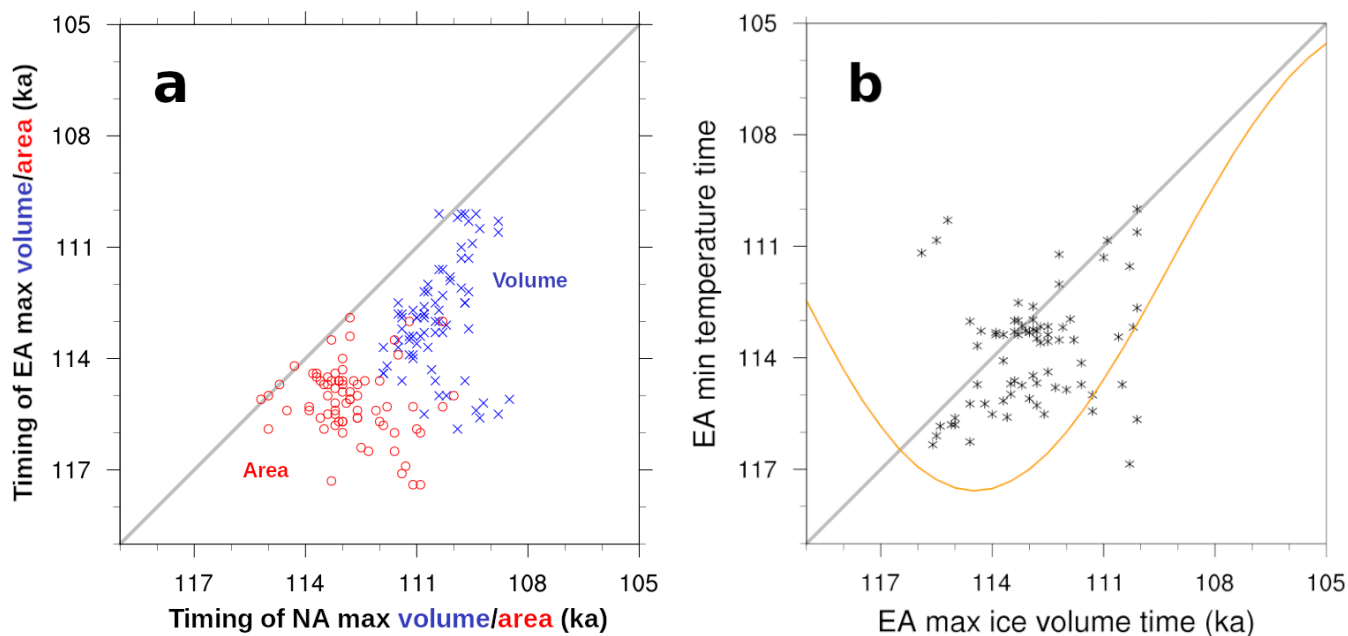


Figure 10. **a.** Timing of the EA ice volume (blue) and area (red) peak with respect to the NA peak time. **b.** Timing of the EA minimum temperature and maximum ice sheet volume for individual runs. The orange curve shows the summer (JJA) insolation at 60°N.

325 regions except for those with high levels of accumulation (*e.g.* the Rockies). NA ice sheet area reaches its maximum after the temperature and precipitation minima, between 114 and 113 ka (see figures 10a and 11). Thus, both temperature and precipitation are increasing at the time that the maximum NA ice sheet area is reached.

NA ice volume continues to grow until approximately 111 ka through a thickening of the ice sheet (*cf.* figure 4) in response to increasing precipitation under continuing cold temperatures. During the 113 to 111 ka interval, the low elevation sectors of the southern NA ice margin in the sample simulation in figure 4 is generally between the 4°C to 2°C JJA isotherms. Eventually, the NA ice sheet begins to lose mass after further increases in temperature and precipitation. At this time, the southern margin of the ice sheet tend to fall south of the 4°C isotherm.

In EA, temperature and precipitation also show an abrupt but weaker reduction in the early inception. The ensemble mean EA summer temperature and precipitation minima have a longer duration interval than that of NA and show little sensitivity to the pCO₂ changes. The reasons for this result are as yet unclear. The onset of renewed EA warming and increasing precipitation correspond to the maximum extent of EA ice sheets. However, EA ice volume continues to grow for as much as another 3 kyr. EA temperature and precipitation gradually increase until ~113 ka, when the sea ice area starts to decline (figure 11). After this time, both temperature and precipitation increases accelerate.

The southern margin of the EA ice sheet largely mirrors NA the relationship to surface isotherms, at least for the sample run in figure 4. During the growth phase, the ice margin tends to lie in between the 2°C to -2°C JJA isotherms. By 109 ka, the EA southern margins are generally south of the 4°C isotherm.

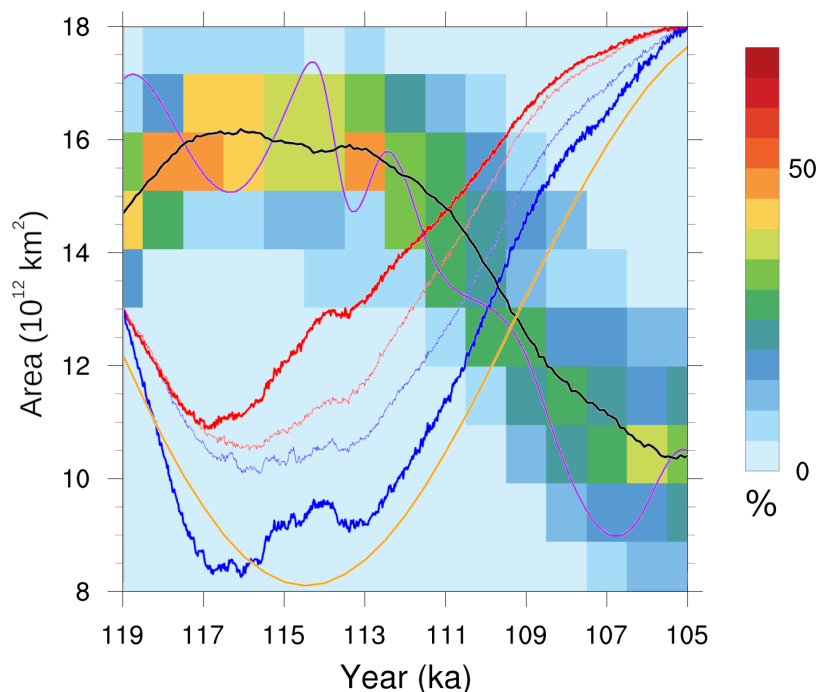


Figure 11. The ensemble distribution of Northern Hemisphere late summer sea ice total area. The black line shows the ensemble mean late summer sea ice area. The blue lines show the scaled ensemble mean summer temperature anomaly with respect to 119 ka in NA (thick) and EA (thin). The red lines show the scaled ensemble mean annual precipitation anomaly with respect to 119 ka in NA (thick) and EA (thin). The orange line represents the summer insolation at 60°N. The purple line shows the changes in $\log(p\text{CO}_2)$ to approximately capture its effective radiative forcing. Temperature, precipitation, insolation, and $p\text{CO}_2$ are plotted solely for the sake of phase comparison, and therefore their actual values are not indicated.

In assessing the contributions of sea ice, the AMOC and the jet stream, summer sea ice has the strongest correlations with temperature and precipitation changes in EA. Late winter sea ice area shows no consistent pattern of change over this time period and is not related to ice sheet volumes in either NA or EA (see supplemental figure 1). However, its summer extent
345 varies in correspondence with Northern Hemisphere temperatures: it peaks prior to the minimum in insolation at 60°N, remains extended, and then decreases. The onset of major sea ice retreat at approximately 113 ka is in phase with a rapid acceleration of both NA and EA summer warming and annual-mean precipitation. Deciphering the causal relationships of this phasing requires future sensitivity experiments. However, one can infer that sea ice likely has a positive feedback role for both precipitation and temperature at this time.

350 Neither the AMOC (supplemental figure 3) nor the wintertime jet stream exhibit any clear consistent changes that coincide with temperature and precipitation or ice sheet changes. In 80% of the runs, the AMOC gradually increases during the glacial inception to a maximum of 22 Sv around 108 ka. After this, it decreases once more to its initial values of 16 to 18 Sv. In the remaining 20% of runs, the AMOC oscillates between two values.

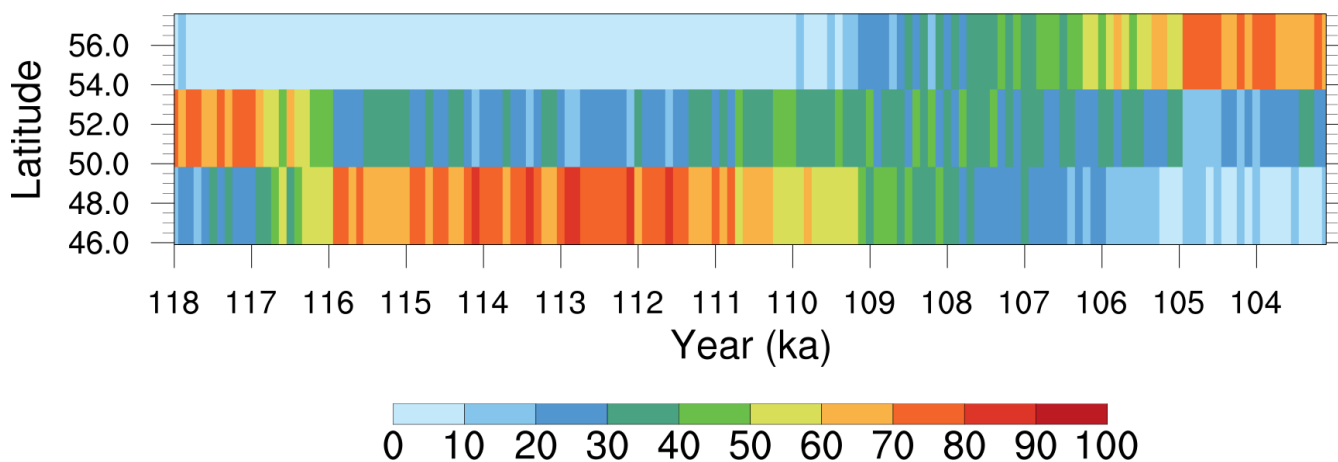


Figure 12. Ensemble distribution of mean most southern latitudinal position of the JJA jet of the Atlantic Ocean.

Similarly, the minimum latitude of the North Atlantic mean winter jet stream is restricted to 43 to 47°N with the only
355 significant change over time being an increase in the fraction of runs with the more southern position (with greater than 70%
of runs by 104 ka). Previous work indicates that the latitudinal position of the winter-time North Atlantic jet stream depends
on the latitude of the south-eastern margin of the NA ice sheet (Andres and Tarasov, 2019). For the current ensemble, the NA
ice sheet remains north of the preferred latitude for the jet stream at all times, so the ice sheet is unable to directly influence the
jet stream in this way.

360 However, the minimum latitude of the summertime North Atlantic jet stream does vary in concert with NA ice sheet and sea
ice extents. Specifically, the majority of runs transition their southern jet position from 52°N to 48°N during the 117 to 116 ka
interval (figure 12), in correspondence with significant initial ice growth over the NA_{Qb} sector (figure 8, this provides the most
proximal sector diagnostic for central and eastern Canada). The subsequent northward migration occurs across the ensemble
from 110 to 107 ka, again in correspondence with the wider cross-ensemble range of deglaciation times for the NA_{Qb} sector.
365 The much warmer JJA temperature during 107 ka compared to 119 ka in figure 1 likely explains the higher latitudinal position
(56°N) of the ensemble mean summer jet at 107 ka compared to that of 118 ka. These shifts in the jet stream likely affect
summertime temperature and precipitation over EA.

4 Discussion

4.1 Caveat about marine sectors

370 Ice sheet growth in marine sectors is found to be highly sensitive to the treatment of sub-shelf melt, even at high latitudes. This
is particularly evident in figure 6, where marine ice sheet margins are at times extended straight lines. These lines match the
boundaries for different ocean temperature sectors in LCice, which propagates the vertical temperature profile from assigned
upstream diagnostic sites to whole downstream ocean sectors for computing submarine ice melt (Bahadory and Tarasov, 2018).



This artifact of the model setup underlines the potentially important role of ocean temperatures on submarine melt and its
375 control of marine ice extent.

The crude shallow ice approximation treatment of ice shelves in the utilized version of the GSM along with the continuing
challenge for the community to find a well constrained ice calving representation are further contributors to uncertainty in the
marine sector results of the model. The GSM has been recently revised with the inclusion of shallow shelf approximation ice
dynamics and ongoing work will examine the impact of this and other model updates on resultant modelled LGI ice evolution.

380 **4.2 Widespread snowfield glaciation versus spreading from high elevation nucleation sites**

Our results provide a sensible merger of the two contrasting hypotheses. Glaciation starts with nucleation over high latitude
and high elevation regions, but widespread snowfield thickening subsequently creates thin ice (< 500 masl) over expanses of
continental northern sectors for both NA (by 118 ka) and EA (between 118 to 117 ka). This is clearly visible for our sample
best fit run (figure 4).

385 **4.3 The challenge of excessive Alaskan glaciation**

The one significant transgression of inferred Late Pleistocene glacial limits in our ensemble is near complete glaciation of
Alaska (figure 5). This is contrary to geological inferences (Kaufman et al., 2011). If the inferences are correct, then the
approximately 4 to 6 m SLE contribution to the inception peak from glaciation of central Alaska in our ensemble should be
removed from our ensemble total.

390 Excessive glaciation of Alaska is a common problem for models (*e.g.* Bonelli et al., 2009). Past studies indicate at least two
factors may resolve this problem: atmospheric model resolution (and/or complexity) and changes in snow albedo due to dust
deposition. Though still displaying somewhat excessive Alaskan ice coverage, Herrington and Poulsen (2011) avoid complete
glaciation with fixed 116 ka boundary conditions using the GENESIS AGCM (and slab ocean) at T31 resolution. A glacial
decrease in surface air pressure over the Bering Strait region is apparently associated with an increase in northward transport
395 of sensible heat towards Alaska. Whether this suppression of Alaskan glaciation is solely due to increased atmospheric model
resolution or complexity is unclear. It is also unclear if the result Herrington and Poulsen (2011) would persist with a fully
coupled ocean model.

Using the CLIMBER EMIC, Ganopolski et al. (2010) obtain reduced though still excessive Alaskan glaciation. A previous
study traced much of this reduction to the inclusion of aeolian dust forcing on snow albedo for the surface mass balance
400 determination (Calov et al., 2005b). However confidence in these results is limited given the crude determination of dust
deposition and associated albedo changes in their model. More advanced studies have verified the significant impact of dust on
snow albedo (Krinner et al., 2006, though with an imposed dust-deposition rate) but have also found it difficult to obtain even
the magnitude of dust deposition (Mahowald et al., 2006) inferred from extensive loess deposits in Alaska (Muhs et al., 2003).
A potentially critical role for changing dust deposition in suppressing Alaskan glaciation is therefore plausible, but in need of
405 more advanced modelling.



4.4 Brief comparison to past geological inferences

To our knowledge, there is no community-based geologically-inferred MIS 5 ice margin reconstruction for NA. Aside from the issue of Alaska (and certain adjacent parts of the Yukon), our results are, within (large) age uncertainties, consistent with the till stratigraphy presented in Clark et al. (1993).

410 Eurasia also lacks a clear geologically-inferred LGI stadial extent. However, the geologically-inferred Early Weichselian (MIS 5) ice extent maximum of Svendsen et al. (2004, nominal 90 ka in) generally encloses (and for much of the southern margin largely tracks) the 50% ensemble distribution (figure 6). The main regional exceptions are more extensive ice on the western coast of Svalbard and extensive marine ice on the western Norwegian coast. We leave it to members of the geological community to execute more detailed and up-to-date comparisons with our ensemble chronologies.

415 4.5 Is there a single very likely spatio-temporal pattern of LGI ice sheet evolution?

To partially characterize the range of the spatio-temporal patterns of ice sheet evolution in our ensemble, we consider the intersectorial relationships of maximum ice volume for each ensemble run (figure 13). The absence of correlation in maximum ice volumes for different sectors will indicate that there are multiple temporal patterns of ice development in these regions.

420 For NA, the northern Arctic (NA_{El}) sector maximum ice volume has no obvious correlation with that of other sectors. This is consistent with the continual growth of ice throughout the simulations in this region. All other NA sectors display relatively strong correlations aside from a threshold response for NA_{Qb} relative to the Pacific Cordillera (NA_{Rc}).

425 For EA, again the most northern and continuously growing sector (EA_{Sv}) has relatively no correlation in maximum ice volume with other sectors (figure 13). The relatively northern and largely marine eastern sector ($EA_{K\tau}$) has a strong correlation with the two Fennoscandian sectors for the 5 runs with maximum ($EA_{K\tau}$) greater than 2.5 mSLE. For the other runs, the correlation is much weaker and with a much lower mean slope, perhaps indicative of a threshold in ocean temperatures controlling subshelf melt and enabling ice calving.

430 There are no strong correlations between NA and EA regions (c.f. supplemental figure 4). There is moderate correlation between the Baffin Island sector NA_{Bf} and western Fennoscandia EA_{WF} , perhaps reflecting ocean circulation connections between Baffin Bay and the GIN Seas. More limited correlation exist between NA_{Bf} and eastern Fennoscandia (EA_{EF} and and between the western Cordillera (EA_{Rc}) and western Fennoscandia EA_{WF}). The only other possible relation of note is the absence of large maximum ice volumes for the eastern Kara Sea region ($EA_{K\tau}$) when ice volumes are near maximal for all NA sectors south of Ellesmere (with only 5 runs for this case, the relationship is tentative).

435 The only clear indication of a bifurcation in regional temporal evolution is the presence of both early and late timing of maximum regional ice volume for Fennoscandia (EA_{EF} and EA_{WF}) for a range of regional maximum ice volumes (figure 8). The extent to which possible associated bifurcations in sea ice extent and stationary atmospheric waves (described in the results section) may play a role in this must await future analysis.

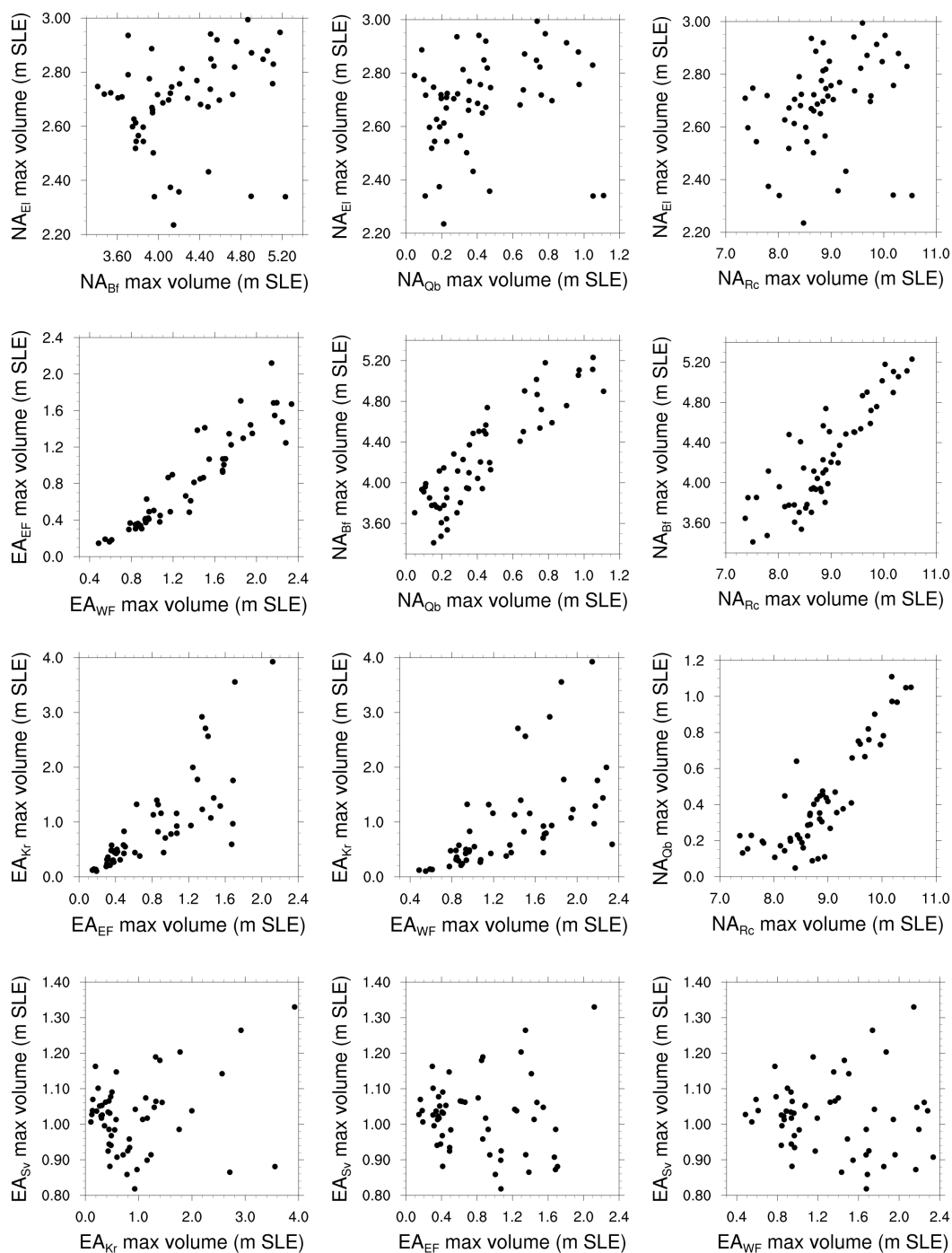


Figure 13. Correlation plots of maximum ice volume for NA and EA diagnostic sectors (figure 7).

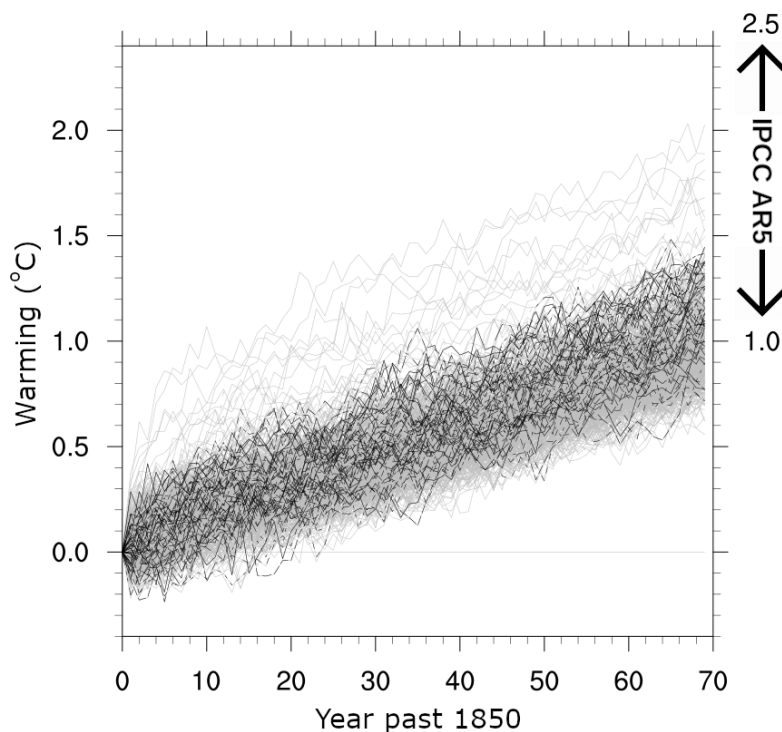


Figure 14. The mean global warming projected by the selected 55 ensemble members (black lines) and the 500 inception simulations (grey lines) in the TCR experiment (refer to the text for details). The model TCR warming range reported in the IPCC AR5 (Flato et al., 2013) is shown on the right axis.

4.6 Transient climate response

The TCR warming of all 500 ensemble members is between 0.6 and 2.0°C in figure 14. The full ensemble therefore brackets the lower bound (0.7°C) but not the upper bound (2.5°C) of the IPCC AR5 multi-model TCR results (Flato et al., 2013)).
440 The constraint of capturing “acceptable” LGI growth and retreat (*i.e.* the “successful” 55 member sub-ensemble) reduces this range to 0.7 to 1.4°C. This range is therefore significantly lower than that of the TCR results in the IPCC AR5. Given the simplified physics, limited climate model resolution of LCice, this reduced upper bound response range requires replication by more advanced models to acquire any significant confidence. However, as is, the result underlines the potential value that LGI replication in coupled ice/climate modelling has for constraining climate model sensitivity and therefore constraining future
445 climate change.

5 Conclusions

We used LCice 1.0, a two-way coupled ice sheet and climate model, to generate an ensemble of 500 transient simulations of the LGI that differ according to the combination of parameters and parameterizations used in the climate component (LOVE-



CLIM), the ice sheet component (the GSM) and the coupling between them. Of these 500 simulations, 55 simulations passed
450 our ice volume evolution acceptance criteria for the LGI. In this paper, we document the patterns of ice growth and retreat
exhibited by North American and Eurasian ice sheets in these 55 runs.

We applied two tests of the representativeness of these simulations to historical changes during the LGI: comparisons of
total sea level changes with time, and comparisons of near-surface air temperatures at the location of the GRIP ice core.
Maximum LGI ice volume is under-estimated in the ensemble relative to that inferred by Lisiecki and Raymo (2005), although
455 it lies within the collective uncertainties of the three proxy reconstructions considered herein. Another possibly significant
discrepancy is the timing of the LGI sea level minimum, with our model ensemble sea level minimum occurring approximately
2 kyr earlier than that of the Lisiecki and Raymo (2005) and Waelbroeck et al. (2002) reconstructions but less than 1 kyr after
the sea level minimum in Siddall et al. (2003). These discrepancies are likely partly due to the absence of a modelled (and
probably out of phase) Antarctic ice sheet contribution in LCice 1.0, and partly due to dating uncertainties in the proxy based
460 reconstructions.

The ensemble-mean temperature is in approximate agreement with an inverse reconstruction from the GRIP ice core during
the LGI cooling phase. Subsequently, a strong warming in the model driven by orbital and greenhouse gas forcing is absent
in the reconstruction. Given regional warming is robust across the ensemble and the lack of a plausible physical mechanism
to sustain cold, stadial conditions under increasing insolation, we suggest the discrepancy may be due in part to uncertainties
465 in the $\delta^{18}\text{O}$ to temperature inversion. This may also explain in part why the model also fails to capture the millennial scale
variance of the proxy record.

The regional LGI pattern of initial ice growth and evolution in NA and EA is consistent with the high elevation and high
latitude nucleation paradigm (first over Ellesmere, Svalbard and Franz Joseph islands, then the northern Rockies, and Baffin and
Novaya Zemlya islands). Subsequent nucleation over lower latitudes is followed by large-scale snowfield expansion/thickening
470 over central northern Canada, merging eastern and western NA ice in all runs.

The EA ice sheet is more sensitive to orbital forcing and ensemble parameters. It varies between a single ice sheet to multiple
ice caps at its peak volume. The peak in the EA ice sheet's volume occurs prior to the NA ice sheet in all runs. The timing
of maximum ice sheet area tends to be 2-3 kyr earlier than that of maximum ice volume for each ice sheet. After the LGI ice
volume peak, retreat happens across most sectors except for continued (though slower) growth in the most northern Ellesmere
475 and Svalbard sectors. Aside from the latter, EA tends to have almost complete ice loss by 104 ka.

The southern margin of both ice sheets generally progress from falling between the 2°C to -2°C JJA isotherms during the
growth phase to a location south of the 4°C during the peak retreat phase. This progression to warmer isotherms is due to a
combination of increasing precipitation and enhanced ice flux to the southern margin (given the thicker upstream ice during the
retreat phase). The post-LGI stadial ice mass loss rate and temperature and precipitation increases in EA have higher correlation
480 with sea ice retreat compared to that for NA ice, temperature, and precipitation.

Two perhaps novel features pertaining to NA and Greenland may be of interest to glacial geologists and paleoceanographers.
The Greenland ice sheet and Icelandic ice cap are connected in all runs by 114 ka. Furthermore, there is an ice bridge between
NA and Greenland across Davis Strait in approximately 80% of ensemble runs. These results have low confidence given



485 limitations in the marine sector of the current version of LCice. Ongoing work with an improved version of LCice will provide
a more confident assessment of the plausibility of these two features.

One other question we examined is the extent to which capture of LGI ice sheet volume response in line with sea level
proxies can constrain the transient climate response of the coupled model to a doubling of atmospheric $p\text{CO}_2$. For our LCice
1.0 ensemble, we find a slight upward constraint on the model lower bound, but a strong reduction of the upper bound of
warming to 1.4°C (from an unconstrained upper bound of 2.0°C).

490 An intended contribution of this study is its ability to foster new research about LGI. We will be making a high variance
subset of the simulations described in this paper publicly available via an online archive for other groups to use. We especially
hope that the field data community will use this archive to test, refute, and/or validate which, if any, of the model-derived
trajectories (and characteristics thereof) for LGI are consistent with the paleo record.



495 *Data availability.* The authors have temporarily archived two sample LGI chronologies (including surface elevation and ice sheet thickness, as well as temperature and precipitation climatologies) for reviewer benefit during the Climate of the Past Discussion phase of submission. These are available at <https://www.physics.mun.ca/~lev/dataAccess.html>. After consideration of reviewer feedback, a larger high variance subset of ensemble runs will be permanently archived on a public server before submission to (non-discussion) Climate of the Past.

500 *Author contributions.* Taimaz Bahadory ran the model ensemble, carried out the ensemble analysis, and wrote the initial draft of this submission. Lev Tarasov conceived the project, co-designed the experimental/analysis plan, and provided extensive editorial contributions. Heather Andres also provided extensive editorial contributions.

Competing interests. The authors have no competing interests.

Acknowledgements. The authors thank Marilena Geng for editorial help. This work was supported by a NSERC Discovery Grant (LT), the Canadian Foundation for Innovation (LT), the Atlantic Computational Excellence Network (ACEnet), the Canada Research Chairs program (LT), and the CREATE training program in Climate Science (LT).



505 References

- Andres, H. J. and Tarasov, L.: Towards understanding potential atmospheric contributions to abrupt climate changes: characterizing changes to the North Atlantic eddy-driven jet over the last deglaciation, *Climate of the Past*, 15, 1621–1646, 2019.
- Andrews, J. and Barry, R.: Glacial inception and disintegration during the last glaciation, *Annual Review of Earth and Planetary Sciences*, 6, 205–228, 1978.
- 510 Andrews, J. and Mahaffy, M.: Growth rate of the Laurentide Ice Sheet and sea level lowering (with emphasis on the 115,000 BP sea level low), *Quaternary Research*, 6, 167–183, [https://doi.org/10.1016/0033-5894\(76\)90048-X](https://doi.org/10.1016/0033-5894(76)90048-X), 1976.
- Bahadory, T. and Tarasov, L.: LCice 1.0 – a generalized Ice Sheet System Model coupler for LOVECLIM version 1.3: description, sensitivities, and validation with the Glacial Systems Model (GSM version D2017.aug17), *Geoscientific Model Development*, 11, 3883–3902, <https://doi.org/10.5194/gmd-11-3883-2018>, <https://www.geosci-model-dev.net/11/3883/2018/>, 2018.
- 515 Bard, E., Hamelin, B., Fairbanks, R. G., and Zindler, A.: Calibration of the ^{14}C timescale over the past 30,000 years using mass spectrometric U/Th ages from Barbados corals, *Nature*, 345, 405–409, 1990.
- Beghin, P., Charbit, S., Dumas, C., Kageyama, M., Roche, D., and Ritz, C.: Interdependence of the Northern Hemisphere ice-sheets build-up during the last glaciation: the role of atmospheric circulation., *Climate of the Past Discussions*, 9, 2013.
- Bonelli, S., Charbit, S., Kageyama, M., Woillez, M.-N., Ramstein, G., Dumas, C., and Quiquet, A.: Investigating the evolution of major Northern Hemisphere ice sheets during the last glacial-interglacial cycle, *Climate of the Past*, 5, 329–345, <https://doi.org/10.5194/cp-5-329-2009>, <https://www.clim-past.net/5/329/2009/>, 2009.
- 520 Calov, R., Ganopolski, A., Claussen, M., Petoukhov, V., and Greve, R.: Transient simulation of the last glacial inception. Part I: glacial inception as a bifurcation in the climate system, *Climate Dynamics*, 24, 545–561, 2005a.
- Calov, R., Ganopolski, A., Petoukhov, V., Claussen, M., Brovkin, V., and Kubatzki, C.: Transient simulation of the last glacial inception. Part II: sensitivity and feedback analysis, *Climate Dynamics*, 24, 563–576, 2005b.
- 525 Calov, R., Ganopolski, A., Kubatzki, C., and Claussen, M.: Mechanisms and time scales of glacial inception simulated with an Earth system model of intermediate complexity, *Climate of the Past*, 5, 245–258, 2009.
- Chappell, J., Omura, A., Esat, T., McCulloch, M., Pandolfi, J., Ota, Y., and Pillans, B.: Reconciliation of late Quaternary sea levels derived from coral terraces at Huon Peninsula with deep sea oxygen isotope records, *Earth and planetary science letters*, 141, 227–236, 1996.
- 530 Clark, P., Clague, J., Curry, B., Dreimanis, A., Hicock, S., Miller, G., Berger, G., Eyles, N., Lamothe, M., Miller, B., Mott, R., Oldale, R., Stea, R., Szabo, J., Thorleifson, L., and Vincent, J.: Initiation and development of the Laurentide and Cordilleran ice sheets following the last interglaciation, *Quat. Sci. Rev.*, 12, 79–114, 1993.
- Colleoni, F., Wekerle, C., Näslund, J.-O., Brandefelt, J., and Masina, S.: Constraint on the penultimate glacial maximum Northern Hemisphere ice topography (140 kyr BP), *Quaternary Science Reviews*, 137, 97–112, 2016.
- 535 Dansgaard, W., Johnsen, S. J., Clausen, H. B., Dahl-Jensen, D., Gundestrup, N. S., Hammer, C. U., Hvidberg, C. S., Steffensen, J. P., Sveinbjörnsdóttir, A. E., Jouzel, J., and Bond, G. C.: Evidence for general instability of past climate from a 250 kyr ice-core record, *Nature*, 264, 218–220, 1993.
- Flato, G., Marotzke, J., Abiodun, B., Braconnot, P., Chou, S. C., Collins, W., Cox, P., Driouech, F., Emori, S., Eyring, V., Forest, C., Gleckler, P., Guilyardi, E., Jakob, C., Kattsov, V., Reason, C., and Rummukainen, M.: Evaluation of Climate Models, in: *Climate Change 2013: The Physical Science Basis. Contribution of Working Group I to the Fifth Assessment Report of the Intergovernmental Panel on Climate*
- 540



- Change, edited by Stocker, T. F., Qin, D., Plattner, G.-K., Tignor, M., and J. Boschung, S. K. A., Nauels, A., Xia, Y., Bex, V., and Midgley, P. M., pp. 741–866, Cambridge University Press, Cambridge, United Kingdom and New York, NY, USA, 2013.
- Gallup, C. D., Cheng, H., Taylor, F. W., and Edwards, R. L.: Direct Determination of the Timing of Sea Level Change During Termination II, *Science*, 295, 310–313, <https://doi.org/10.1126/science.1065494>, <https://science.sciencemag.org/content/295/5553/310>, 2002.
- 545 Ganopolski, A., Calov, R., and Claussen, M.: Simulation of the last glacial cycle with a coupled climate ice-sheet model of intermediate complexity, *Climate of the Past*, 6, 229–244, 2010.
- Goosse, H., Renssen, H., Timmermann, A., and Bradley, R. S.: Internal and forced climate variability during the last millennium: a model-data comparison using ensemble simulations, *Quaternary Science Reviews*, 24, 1345–1360, 2005.
- Goosse, H., Driesschaert, E., Fichet, T., and Loutre, M.-F.: Information on the early Holocene climate constrains the summer sea ice
550 projections for the 21st century, *Climate of the Past*, 3, 683–692, <https://hal.archives-ouvertes.fr/hal-00298097>, 2007.
- Herrington, A. R. and Poulsen, C. J.: Terminating the Last Interglacial: The role of ice sheet–climate feedbacks in a GCM asynchronously coupled to an ice sheet model, *Journal of climate*, 25, 1871–1882, 2011.
- Kageyama, M. and Valdes, P. J.: Impact of the North American ice-sheet orography on the Last Glacial Maximum eddies and snowfall, *Geophysical Research Letters*, 27, 1515–1518, 2000.
- 555 Kaufman, D., Young, N., Briner, J., and Manley, W.: Alaska Palaeo-Glacier Atlas (Version 2), in: Quaternary Glaciations Extent and Chronology, Part IV: A Closer Look, edited by Ehlers, J. and Gibbard, P., no. 15 in *Developments in Quaternary Science*, pp. 427–445, Elsevier, 2011.
- Krinner, G., Boucher, O., and Balkanski, Y.: Ice-free glacial northern Asia due to dust deposition on snow, *Climate Dynamics*, 27, 613–625, 2006.
- 560 Lambeck, K. and Chappell, J.: Sea level change through the last glacial cycle, *Science*, 292, 679–686, 2001.
- Liakka, J., Löfverström, M., and Colleoni, F.: The impact of the North American glacial topography on the evolution of the Eurasian ice sheet over the last glacial cycle, 2016.
- Lisiecki, L. E. and Raymo, M. E.: A Pliocene-Pleistocene stack of 57 globally distributed benthic $\delta^{18}\text{O}$ records, *Paleoceanography*, 20, <https://doi.org/10.1029/2004PA001071>, <https://agupubs.onlinelibrary.wiley.com/doi/abs/10.1029/2004PA001071>, 2005.
- 565 Mahowald, N. M., Muhs, D. R., Levis, S., Rasch, P. J., Yoshioka, M., Zender, C. S., and Luo, C.: Change in atmospheric mineral aerosols in response to climate: Last glacial period, preindustrial, modern, and doubled carbon dioxide climates, *Journal of Geophysical Research: Atmospheres*, 111, 2006.
- Morzadec, K. L. and Tarasov, L.: The impact of fjords on ice sheets and their subgrid representation in models, *The Cryosphere Discuss.*, 2017.
- 570 Muhs, D. R., Ager, T. A., Bettis III, E. A., McGeehin, J., Been, J. M., Begét, J. E., Pavich, M. J., Stafford Jr, T. W., and De Anne, S.: Stratigraphy and palaeoclimatic significance of Late Quaternary loess–palaeosol sequences of the Last Interglacial–Glacial cycle in central Alaska, *Quaternary Science Reviews*, 22, 1947–1986, 2003.
- Pollard, D. and PMIP-participating groups: Comparisons of ice-sheet surface mass budgets from Paleoclimate Modeling Intercomparison Project (PMIP) simulations, *Glob. and Planet. Change.*, 24, 79–106, 2000.
- 575 Renssen, H., Seppä, H., Heiri, O., Roche, D., Goosse, H., and Fichet, T.: The spatial and temporal complexity of the Holocene thermal maximum, *Nature Geoscience*, 2, 411–414, 2009.



- Roche, D. M., Dokken, T. M., Goosse, H., Renssen, H., and Weber, S. L.: Climate of the Last Glacial Maximum: sensitivity studies and model-data comparison with the LOVECLIM coupled model, *Climate of the Past*, 3, 205–224, <https://hal.archives-ouvertes.fr/hal-00298075>, 2007.
- 580 Siddall, M., Rohling, E. J., Almogi-Labin, A., Hemleben, C., Meischner, D., Schmelzer, I., and Smeed, D.: Sea-level fluctuations during the last glacial cycle, *Nature*, 423, 853–858, 2003.
- Stokes, C. R., Tarasov, L., and Dyke, A. S.: Dynamics of the North American Ice Sheet Complex during its inception and build-up to the Last Glacial Maximum, *Quaternary Science Reviews*, 50, 86–104, 2012.
- Svendsen, J. I., Alexanderson, H., Astakhov, V., Demdov, I., Dowdeswell, J., Funder, S., Gataullin, V., Henriksen, M., and Hjort, C.: Late
585 Quaternary ice sheet history of northern Eurasia, *Quat. Sci. Rev.*, 23, 1229–1271, 2004.
- Tarasov, L. and Peltier, W. R.: Terminating the 100 kyr Ice Age cycle, *jgr*, 102, 21 665–21 693, 1997a.
- Tarasov, L. and Peltier, W. R.: A high-resolution model of the 100 kyr Ice Age cycle, *Ann. Glaciol.*, 25, 58–65, 1997b.
- Tarasov, L. and Peltier, W. R.: Greenland glacial history and local geodynamic consequences, *Geophys. J. Int.*, 150, 198–229, 2002.
- Tarasov, L. and Peltier, W. R.: Greenland glacial history, borehole constraints and Eemian extent, *J. Geophys. Res.*, 108, 2124–2143, 2003.
- 590 Tarasov, L. and Peltier, W. R.: A calibrated deglacial drainage chronology for the North American continent: Evidence of an Arctic trigger for the Younger Dryas, *qsr*, 25, 659–688, 2006.
- Tarasov, L. and Peltier, W. R.: The Co-evolution of continental ice cover and permafrost extent over the last glacial-interglacial cycle in North America, *JGR-Earth Surface*, 112, doi:10.1029/2006JF000 661, 2007.
- Tarasov, L., Dyke, A. S., Neal, R. M., and Peltier, W. R.: A data-calibrated distribution of deglacial chronologies for the North American ice
595 complex from glaciological modeling, *epsl*, 315-316, 30–40, 2012.
- Ullman, D. J., LeGrande, A. N., Carlson, A. E., Anslow, F. S., and Licciardi, J. M.: Assessing the impact of Laurentide Ice Sheet topography on glacial climate, *Climate of the Past*, 10, 487–507, <https://doi.org/10.5194/cp-10-487-2014>, <https://www.clim-past.net/10/487/2014/>, 2014.
- Waelbroeck, C., Labeyrie, L., Michel, E., Duplessy, J. C., McManus, J., Lambeck, K., Balbon, E., and Labracherie, M.: Sea-level and deep
600 water temperature changes derived from benthic foraminifera isotopic records, *Quaternary Science Reviews*, 21, 295–305, 2002.
- Weertman, J.: Rate of growth or shrinkage of nonequilibrium ice sheets, *Journal of Glaciology*, 5, 145–158, 1964.